Smart co-delivery of miR-34a and cytotoxic peptides (LTX-315 and melittin) by chitosan based polyelectrolyte nanocarriers for specific cancer cell death induction

Smart co-delivery of miR-34a and cytotoxic peptides (LTX-315 and melittin) by chitosan based polyelectrolyte nanocarriers for specific cancer cell death induction

Marjan Motiei[a,b], Fatemeh Aboutalebi[a], Mahboobeh Forouzanfar[a], Kianoush Dormiani[a], Mohammad Hossein Nasr-Esfahani[a,*], Seyede Zohreh Mirahmadi-Zare[a,*]

[a]*Department of Animal Biotechnology, Cell Science Research Center, Royan Institute for Biotechnology, ACECR, 8159358686 Isfahan, Iran*

[b]*Centre of Polymer Systems, Tomas Bata University in Zlín, Tšída Tomáše Bati 5678, 76001 Zlín, Czech Republic*

[*]*Corresponding authors: E-mail addresses: mh.nasr-esfahani@royaninstitute.org (M.H. Nasr-Esfahani), mirahmadi_zare@royaninstitute.org (S.Z. Mirahmadi-Zare).*

ABSTRACT

A novel polyelectrolyte nanocarrier was synthesized via layer-by-layer self-assembly of polycationic and polyanionic chains. The nanocarrier is composed of polyglutamate grafted chitosan core, dextran sulfate as a com-plexing agent, and polyethyleneimine shell decorated with folic acid. This polyelectrolyte complex has unique physicochemical properties so that the core is considered as an efficient carrier for LTX-315 and melittin peptides, and the shell is suitable for delivery of miR-34a. The spherical nanocarriers with an average size of 123 ± 5 nm and a zeta potential of — 36 ± 1 mV demonstrated controlled-release of gene and peptides ensured a synergistic effect in establishing multiple cell death pathways on chemoresistance human breast adenocarcinoma cell line, MDA-MB-231. In vitro cell viability assays also revealed no cytotoxicity for the nanocarriers, and an IC50 of 15 pg/mL and 150 pg/mL for melittin and LTX-315, respectively, after 48 h, whereas co-delivery of melittin with miR-34a increased smart death induction by 54%.

Keywords: Polyelectrolyte nanocarrier, polyglutamate grafted chitosan, gene-peptide co-delivery, miR-34a, LTX-315, melittin, active targeting

1. Introduction

Breast cancer is the most common malignancy in females that can disrupt normal biological processes by invasion of the adjacent tissues and metastasis to distant ones [**1**]. Chemotherapeutics is the first promising option for cancer treatment, but their effectiveness is severely challenged by poor water solubility, lack of targeting capability, nonspecific distribution, systemic toxicity, low therapeutic index, and multidrug resistance (MDR). MDR is a major hurdle in cancer treatment and leads to unsustainable treatment benefits [**2**]. Considering all aspects, it is necessary to develop a novel strategy for drug delivery to induce specific deaths engineered with passive and active targeting. It is hypothesized that toxic cargos (e.g. small molecules, peptides, and microRNA) delivered via a nano-therapeutic carrier are able to exert their cytotoxic effects through different mechanisms such as prolongation of the circulatory half-life, MDR suppression of cancerous cells, and improvement of biodistribution,

bioavailability and controlled release of labile drugs, while reducing immunogenicity and systemic toxicity in healthy tissues.

Recently, microRNAs have been proposed as a novel class of gene-regulatory molecules involved in many critical biological functions, including cell proliferation, development, apoptosis, autophagy, and even tumorigenesis [**3**]. Dysregulation of miRNAs has been recognized as a hallmark of cancer cells, particularly cancer stem cells [**4**]. miR-34a is one of the best characterized tumor-suppressor miRNAs during tumor initiation and progression. It is commonly downregulated in multiple types of cancers, such as breast cancer. miR-34a serves an important function in the p53 pathway and is involved in proliferation, invasion, and metastasis of breast cancer cells [**4**].

LTX-315 is a 9-mer cationic amphiphilic peptide derived from bovine lactoferricin (LfcinB). It has been recognized as a strong inducer of anticancer immune responses in mice and is a selective anticancer agent in preclinical studies with high effectiveness against both drug-resistant and drug-sensitive cancer cells, and lower activity toward normal cells [**5**]. LTX-315 induces necrosis and mitophagy by membranolytic activity and interruption of both the inner and outer membranes of mitochondria [**6**].

Melittin (Mel) is a water-soluble cationic peptide with 26 amino acids and α-helical structure derived from bee venom with a very high membrane-disrupting activity, especially in excitable tissues like nerves and glands. It possesses multiple biological effects, including pain-relief, anti-rheumatoid arthritis, radioprotector, anti-inflammatory, antibacterial, antiviral, anticancer, and immunomodulator properties. It is known that Mel is integrated into lipid membranes and oligomerized into toroidal or barrel stave structures to facilitate pore formation that affects transport pumps, particularly H^+/K^+-ATPase and Na^+/K^+-ATPase, and finally gives rise to cell death. It can also inhibit cell proliferation by downregulation of cyclin D1 and CDK4 expression. The other cytotoxic effect of Mel is induction of apoptosis by downregulation of antiapoptotic Bcl2 and upregulation of proapoptotic p53, Bax, and caspase-3 genes, which are controlled through Akt inactivation and inhibition of the PI3K/Akt signaling pathway [**7**].

There are a few in-vivo studies that have simultaneously used Mel [**8**] or LTX-315 [**9**] with chemotherapeutic drugs to reduce the resistance of cancer cells through their membranolytic properties and to reduce the effective dose using synergistic therapy. However, these systems still suffer from some drawbacks, particularly instability, nontargeting, and uncontrolled release of the cytotoxic peptides in vitro and in vivo. Therefore, it is crucial to introduce a biocompatible targeted nanocarrier capable of delivering simultaneously these cytotoxic peptides with other therapeutics. In this regard, the layer-by-layer polyelectrolyte nanostructures assembled through sequential adsorption of oppositely charged chains provide stable multilayers carrier to encapsulate payloads and promote a sustained release of the cargos. These polyelectrolyte nanocarriers (PENs), based on their components, are potentially cable of capturing different types of molecules with a wide range of size and physicochemical properties.

Chitosan (CS) represents the most promising cationic biopolymer composed of D-glucosamine and N-acetyl-D-glucosamine, linked by β-(1,4)glycosidic bonds, which is utilized in controlled delivery and targeting due to some properties such as biocompatibility, low toxicity, antibacterial properties, and feasible biodegradability [**10**]. The only limiting factor is low aqueous solubility, which can be overcome by protonation of its amino groups in acidic media resulting in a cationic polysaccharide with high charge density [**11**]. There are several examples of chemically [**12**] and physically **[11]** modified CS to develop tailored carriers for controlled delivery of selected cargo.

Polyglutamic acid (PGA) is an unusual anionic poly-amino acid, which is biodegradable, water-soluble, non-immunogenic, edible, and non-toxic for humans and the environment [**13**]. It consists of repetitive

glutamic acid units (i.e., D-glutamic acid, L-glutamic acid, or both) linked by amide linkages [**13,14**]. PGA, with an isoelectric point of about 2.19, forms stable intermolecular complexes with other oppositely charged biopolymers such as CS with an isoelectric point of 6.5 to create the self-assembled polyelectrolyte complexes that can be used in protein delivery [**14**]. Nonetheless, under physiological conditions, these PENs are collapsed or aggregated because of the deprotonation of CS and weakening of the polyion complex [**13**]. Recently, some studies have denoted the use of multi-ion-cross-linkages such as dextran sulfate (DS), tripolyphosphate (TTP) and magnesium sulfate (MgSO4) to increase the stability of PENs over a wider pH range [**13**].

Among the cationic polymers, polyethyleneimine (PEI) is one of the most efficient cationic polymers. It has been employed for gene delivery because of high transfection efficiency and high capability of endosomal escape based on its intrinsic "proton sponge effect". Transfection efficiency and cytotoxicity of PEI are related to its molecular weight. Low molecular weight PEI has been proven to present low cytotoxicity but poor transfection efficiency [**15**]. To address the targeted delivery, PEI also contains sufficient amino groups for a wide array of chemical modifications that can be used for various applications such as active targeting.

Folic acid (FA) is a small molecule, which is accepted as a desirable choice among various types of ligands. FA receptors, especially FRa, are well-known as tumor-associated proteins and are expressed to a greater extent in numerous solid tumors than normal tissues. Thus, FA is considered as a suitable ligand for active targeting [**16**]. In this case, the FRa can actively internalize FA-targeted nanocarriers via the natural process of endocytosis by high affinity (K_d ~0.1-1 nmol/L) [**17**].

In the present study, we developed an innovative targeted multilayer polyelectrolyte nanocarrier containing, LTX-315 and Mel peptides and miR-34a against MDA-MB-231 as an aggressive form of breast cancer with limited treatment options. The proposed carrier are composed of a core with PGA grafted CS, in the presence of uncharged surfactants to increase core stability against pH variation and improve the protein loading capacity. The shell contained DS as a cross-linker and PEI decorated with FA as an approach to improve cellular uptake and transfection efficiency of the nanocarrier. Furthermore, the synergistic effect of Mel/miR-34a on the induction of the different cell death pathways was assessed by investigation of gene silencing of Bcl-2 and Cyclin D1, caspase-8 activation, and DAPI staining.

2. Material and methods

For a detailed explanation of Material and methods refer to Supporting Information section.

2.1. Synthesis and characterization of PGA grafted CS

PGA grafted CS (PGA-CS) was synthesized at the molar ratio of $[NH_2]/[COOH]$ = 3/2 according to previous reported protocol [**18**]. In brief, the mixture of PGA, EDC, and Sulfo-NHS at a molar ratio of [EDC] = [Sulfo-NHS] = 1.5[COOH] in PBS (10 mM, pH 6.0) was added to CS solution (pH 5.0) under stirring at 800 rpm for 30 min at 4 °C and then 24 h in room temperature (RT). Thereafter, the resulted purified freeze-dried copolymer was analyzed by ATR-FTIR spectroscopy (Thermo Nicolet AVATAR 370 FTIR, resolution 8 cm^{-1}, 64 scans) to confirm the coupling reaction.

2.2. Synthesis and characterization of FA grafted PEI

FA grafted PEI was synthesized at a molar ratio of [NH_2]/ [COOH]:20/1. Briefly, the FA was dissolved in alkaline PBS to obtain a solution of 10 mM (pH 9.0), and then the pH was adjusted to 7.4. Afterward, EDC and sulfo-NHS at a molar ratio of 1:1 respect to [COOH] were added to the FA solution under stirring (800 rpm, 2 h, RT). The solution was added to the PEI solution (PBS 10 mM, pH 7.4) under continuous stirring at RT for 24 h. The crude product at pH 9.0 was purified by dialysis (0.5-1.0 kDa MWCO) against deionized water for 72 h. Finally, the freeze-dried pale yellow powder of FA-PEI was characterized by ATR-FTIR spectroscopy.

2.3. Preparation and characterization of FA-PENs and miRNA/peptide-loaded FA-PENs

For the synthesis of miRNA/peptide-loaded FA-PENs, initially, polyelectrolyte core obtained from **Section 2.1** was dispersed in PBS (1.0 mM, pH 4.0, and 0.5% Tween 20) and then ultrasonicated at 90 W for 30 s. The peptide (in PBS 1.0 mM, pH 4.0) was loaded into the core upon incorporation to the core solution under stirring (500 rpm, 30 min, RT). Subsequently, the negatively charged DS solution (1.0 mg/mL, pH 5.5) was added to the core solution ([DS]/[CS] = 2) as a complexing agent under continuous stirring (500 rpm, 30 min, RT). In parallel, the miRNA solution was added rapidly to an aqueous solution of FA-PEI at pH 8.0, mixed by vortexing for 6 s and incubated for 30 min at RT prior to use. Subsequently, it was added to the core coated by DS at a molar ratio of [PEI]/[CS] = 1/2, vortexed for 6 s, and then allowed to stand at RT for 30 min. After each step and before adding the next reagent, the mixture was centrifuged at 7500 rpm for 1 min to remove the excess reagent.

For the preparation of PENs, the process described above was similarly, except for the addition of payloads. Finally, the particle size, zeta potential, and morphology of PENs were measured at 25 °C using dynamic light scattering (HORIBA SZ-100) and SEM (KYKY-EM3200). The Physical stability of nanocarriers was also evaluated based on a change in size and zeta potential after one-month storage at 4 °C.

3. Result and discussion

The smart PEN was developed to synchronize delivery of polycationic peptides and polyanionic genes that potentially induce different pathways of cell death. Referring to this approach, PGA was grafted onto CS to provide appropriate physicochemical properties for peptide delivery. The physicochemical properties of PGA-CS was fully described in our previous work [**18**]. The covalent linkage can provide a more stable core against pH variation as well as site-specific protein loading capacity. It decreases the aggregation or collapse of PENs due to the deprotonation of CS and weakening the polyionic complex. In addition, using the biodegradable and biocompatible negatively charged branched polyanions such as DS can increase the complex stability over a wider range of pH. Therefore, DS was used to compress the polyelectrolyte complex and control the release rate. Subsequently, PEI as the gene carrier was wrapped on the surface of the polyelectrolyte core, while FA was chemically bonded to PEI to identify the folate receptors on the target cell surface. It is expected that the assembly of low molecular weight PEI to other degradable and biocompatible polymers can be an effective approach to combine the beneficial features of maintaining biodegradability and low cytotoxicity. Additionally, this assembly preserves the gene condensing capability as well as transfection efficiency [**19**]. The schematic steps of PEN synthesis and its nanostructure are shown in **Fig. 1**.

3.1. FA-PENs characterization

The nanoconstructs were fabricated by Layer-by-layer self-assembly of oppositely charged layers through electrostatic interactions. Therefore, the zeta potential analysis is the power technique to follow the core/shell structure of the nanocarrier. Although the confocal microscopic image is the strongest evidence to prove the core-shell structure of fluorescent nanocarrier, unfortunately we were unable to provide this data due to the limited size of the nanocarrier. According to the reference text, the confocal microscope with light scattering characteristics, developed by Ernst Abe in 1873, has a limit of 250 nm. Furthermore, due to the soft structure of the nanocarrier, TEM images do not provide good resolution more than SEM for layer boundary distinguish. Therefore, the nanoconstructs were characterized in terms of morphology, size, and size distribution using SEM. As revealed in **Fig. 2A**, the core showed spherical shapes, but there was a great tendency to form larger and more irregular particles in the form of agglomerates during the addition of DS to the core that was also verified by heterogeneous size distribution (**Fig. 2B**). These aggregated particles can be produced by polyelectrolytes unbound to the nanocarriers floating freely in the suspension [**20**]. It is interesting that after the addition of the last layer of FA-PEI in **Fig. 2C**, the number of aggregated particles was diminished, and they showed a propensity to cubic particles with a soft surface texture. Accordingly, the size distribution of core and FA-PENs was obtained to be 90 ± 18 and 106 ± 32 nm, respectively, as shown in **Fig. 2**D and E.

Furthermore, the hydrodynamic size, polydispersity, and surface charge were characterized using DLS. As shown in **Fig. 2F**, the hydrodynamic size of the core was the highest in comparison with each added layer. This result can be explained through the swelling of the core containing ionizable groups and amide bonds. López-León et al. showed that the polymer-based nanocarriers containing ionizable groups exhibit dramatic changes in their swelling behavior, network structure, and permeability in response to pH variation. Ionizable groups showed an additive effect on the diameter of the nanocarriers when pH decreased from 7.0 to 4.0 [**21**]. Salt concentration also affects the swelling degree of hydrogels composed of polyamine acids due to the reduction of the charge shielding effect of ions by amide groups [**22**]. Therefore, the preparation of core in pH 4.0 and salt concentration of 10^{-3} M seems to be critical reasons for its larger size. Moreover, there is a sufficient positive charge on the core surface to support the layer-by-layer architecture by negatively charged DS and further FA-PEI as the positive polyelectrolyte. Adding DS and then FA-PEI resulted in more compact structures and smaller particle sizes. This feature is due to deswelling behavior and strong intermolecular electrostatic interaction among oppositely charged polyelectrolytes caused by increasing pH and decreasing salt concentration. However, there was a tendency toward a wide size distribution with the addition of DS and significant size reduction by the use of FA-PEI. This reduction can be attributed to electrolytic repulsion in layer-by-layer polyelectrolyte nanostructures, which improves the colloidal stability of the nanostructures [**20**]. Also, the different sizes of particles in SEM and DLS can be explained considering the diffusion of H_2O and swelling behavior of the PENs in aqueous media.

In addition to affecting the integrity of polyelectrolyte particles, the surface charge is involved in some characteristics of nanocarriers, such as the stability of the particles due to attractive and repulsive electrostatic forces, the interaction and uptake with cells and also assessing the dominated component on the surface of the particles. As shown in **Fig. 2F**, the zeta potential of the core was positive (+29.2 ±

3.4 mV), which was in accordance with the molar ratio of $[NH_2]/[COOH]$ = 3/2. For the interaction between core and FA-PEI shell, DS was used to reverse the surface charge of the core.

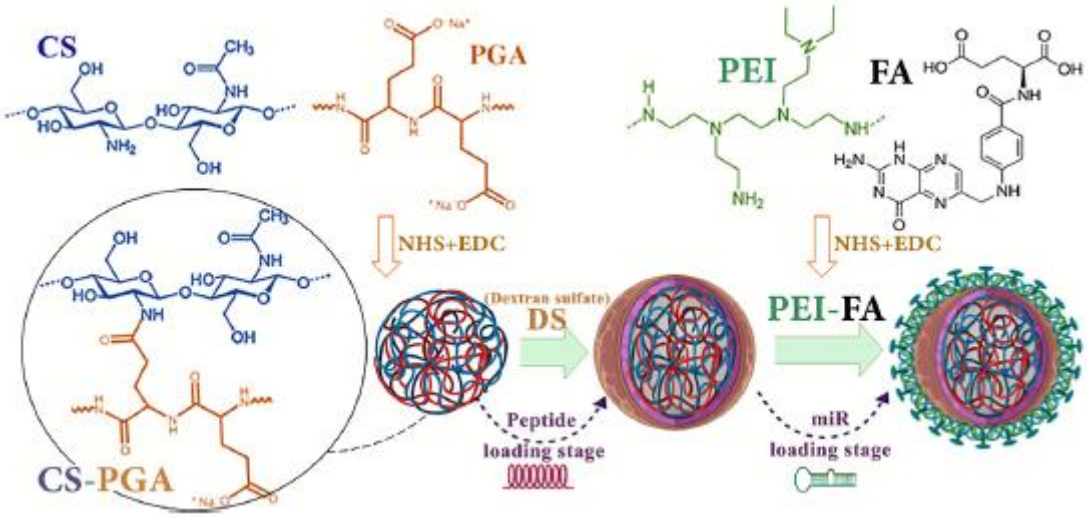

Fig. 1. Schematic description of the synthesis of FA-PENs and peptide and gene loading.

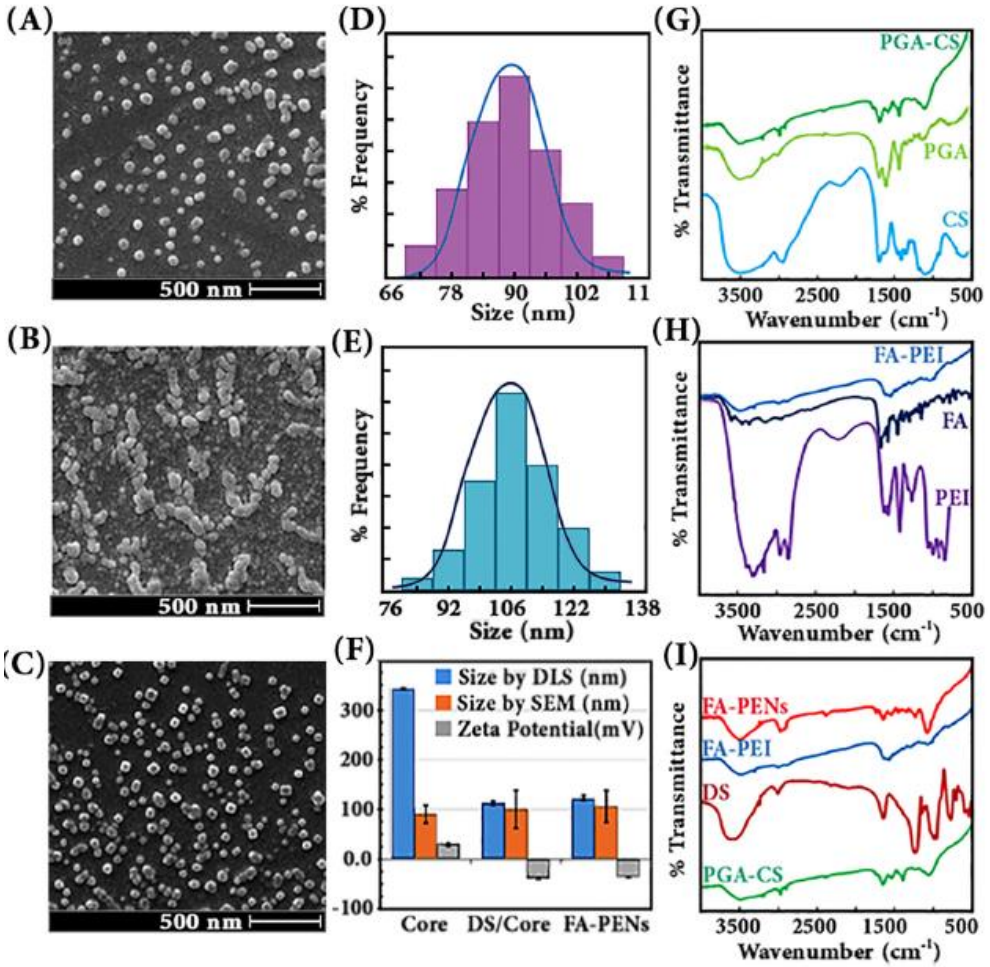

Fig. 2. SEM images of core (A), core/DS (B) and FA-PENs and related size distribution of core (D) and FA-PENs (E); The comparison of size and zeta potential of FA-PENs during the preparation steps (F); The FT-IR spectra of various parts of the core composed of CS, PGA and PGA-CS (G), The shell composed of PEI, FA and FA-PEI (H) and the core/shell including PGA-CS, DS, FA-PEI and FA-PENs (I).

The reduction of zeta potential from high positive to high negative values (—39.5 ± 1.8 mV) confirmed the presence of DS on the core. The addition of FA-PEI to the core/DS caused a slight increase in zeta potential to — 36.9 ± 1.4 mV that was associated to the concentration of FA-PEI.

Since the functional groups and the electrostatic interactions of anionic and cationic polymers change over the layer-by-layer assembling of PENs, ATR-FTIR spectroscopy was used to monitor the accuracy of the synthesis steps. Grafting of PGA onto CS was verified by comparing the infrared spectrum of CS-PGA copolymer with the spectra of neat CS and PGA (**Fig. 2G**). In the characteristic peaks of PGA, shown in **Fig. 2G**, the broad peak at about 2500-3600 cm^{-1} corresponded to the stretching vibration of N—H while the sharp bands at 1570 and 1655 cm^{-1} corresponded to the C—O stretching vibration in the carboxylic acid and amide groups of PGA, respectively [**23—25**]. IR spectra of CS powder also showed two peaks around 899, and 1157 cm^{-1} corresponding to saccharide structure and the other characteristic peaks were assigned to 3450 (OH and NH_2 stretching), 2889 (—CH stretching), 1659 (amide I), 1597 (amide II), 1381 (C—N stretching), and 1095 cm^{-1} (asymmetric C—O—C stretching). The CS-PGA copolymer maintained the original CS pattern, especially since both polymers have similar functional groups that overlap in the FT-IR spectrum. However, successful grafting was further supported by the appearance (or presence) of amide I and amide II bands at 1655 and 1543 cm^{-1} with small shoulders, confirming amidation reaction between free carboxyl groups in PGA and amino groups in CS [**26**].

To ensure the grafting of FA onto PEI, IR spectra were recorded to characterize FA, PEI, and FA-PEI, separately. As shown in **Fig. 2H**, FT-IR spectra of PEI exhibited the characteristic absorption peaks of amine groups located at 3360 and 1651 cm^{-1} and stretching vibration of C—H bonds of the alkyl chain at 2947 and 2843 cm^{-1} [**27,28**]. The characteristic IR absorption peaks at 1605, 1693, and 1485 cm^{-1} in the spectrum of FA were related to the vibration of NH in the CONH group, carbonyl of amide group, and absorption band of the phenyl ring, respectively. While in the FTIR spectrum of FA-PEI, the bands at 1639 and 1581 cm^{-1} were ascribed to amide I and amide II bonds, which attributed to the conjugation of FA onto the surface of PEI. The shift in the carbonyl peak of FA from 1693 cm^{-1} to 1639 cm^{-1} (seen as a small shoulder) also suggested the formation of the linkage. This small shoulder was due to the small amounts of FA [**29**].

Furthermore, in the analysis of FA-PENs spectra (**Fig. 2I**), a small amount of FA-PEI was evident in the structure with a small shoulder corresponding to type I and II amides at 1654 and 1542 cm^{-1}. Also, in comparison with pure DS, the appearance of a sharp peak near 1107 cm^{-1} and the shift of asymmetric stretch of S=O from 1260 to 1249 cm^{-1} indicated the formation of sulphones between oppositely charged sulfo-ions and amines [**30,31**]. However, the peaks of asymmetric and symmetric S—O—S vibrations at about 813 and 582 cm~1 have been diminished in the FA-PENs. It seems that the ionic interactions between amino and sulfate groups resulted in attenuation or shift in the sulfate peaks [**32**].

3.2. Loading characterization

After confirming the correct construction of the nanocarrier, it was independently loaded by peptide and miRNA into the core and shell, respectively. In the first stage, the loading capacity (LC) and encapsulation efficiency (EE) of LTX-315 and Mel were characterized in FA-PENs at the concentration of 50 pg/mL. The results confirmed that the strong electrostatic interaction between PGA-negative carboxyl groups (pI 2.19) and cationic peptides provided high EE (83.6 ± 2.49 and 97.67 ± 1.76) and LC (1.40 ± 0.17 and 1.46 ± 0.41) for Mel and LTX-315, respectively. The higher EE of Mel than LTX-315 in constant concentration can be attributed to the different structure of peptides.

miRNAs loaded cationic vectors are very unstable against negatively charged molecules in serum, which is one of the pressing difficulties in systemic administration for efficient gene silencing [**33**]. Therefore, it is crucial to prepare negatively charged carriers that can entrap a high amount of miRNAs and also protect them from serum degradation. Herein, gel retardation assay was done to evaluate miRNA mobility after the interaction to PEI in positively charged FA-PEI and negatively charged FA-PENs [**34**]. As demonstrated in **Fig. 3A**, naked miRNA as a negative control showed a sharp band compared to the other bands that their intensity was reduced with increasing N/P ratios. It also confirmed that miRNA was entrapped in the well containing FA-PENs and completely disappeared in the supernatant. Therefore, the retarded movement of miRNA entrapped in the nanocarriers on agarose gel showed that FA-PEI and FA-PENs, as delivery carriers, can condense miRNA efficiently.

Besides, to address the ability of the carrier to protect its payload from degradation by serum nucleases which is an important property for efficient nucleic acid delivery into the cells [**34**], serum protection test of naked miRNA and miRNA-loaded nanocarriers was performed in the presence of 5, 10 and 15% FBS by incubating them at 37 °C for 30 min. In **Fig. 3B**, there are bright wells with no trailing bands for the pellets and no bright bands for the supernatant of miRNA-loaded nanocarriers, indicating that miRNA successfully interacted with the nanocarriers and is protected from degradation by serum nucleases. As 30 min was not sufficient for in vitro evaluation of serum stability, in additional experiments, the stability of miRNA was tested using 15% FBS at different time intervals. As shown in **Fig. 3C**, naked miRNA started to degrade as early as 2 h, and most of the miRNA was degraded 8 h post-incubation. While the nanocarriers effectively protected miRNA from nuclease degradation up to 8 h as is demonstrated by bright wells without bright trailing bands. For free miRNA, there were other high dense trailing bands in the presence of FBS that contributed to the interaction between RedSafe and the components in FBS.

3.3. Physical stability studies

Due to the presence of several polyelectrolyte layers in the structure of colloidal nanocarriers, they tend to accumulate when stored in liquid medium. Therefore, the repulsive forces among the particles should be strong enough to resist aggregation and, in turn, improve their stability [**35**]. Herein, the average size, polydispersity, and zeta potential of the FA-PENs stored at 4 °C for one month were measured by DLS to verify the stability of colloidal dispersion. Comparison of the values depicted in Fig. 3D before and after one month of incubation showed that the particle size of suspended particles increased by less than 17% during one month of storage, which was associated with a 9% decrease in the absolute particle surface charge. Although the change in polydispersity of suspended particles was less than 13%, the increase in the size distribution of the nanocarriers after one month was not substantially significant. Concluding, the high surface charge of the nanocarriers with an absolute value >25 mV and coating of the core with multiple layers might lead to physical stability in aqueous solutions.

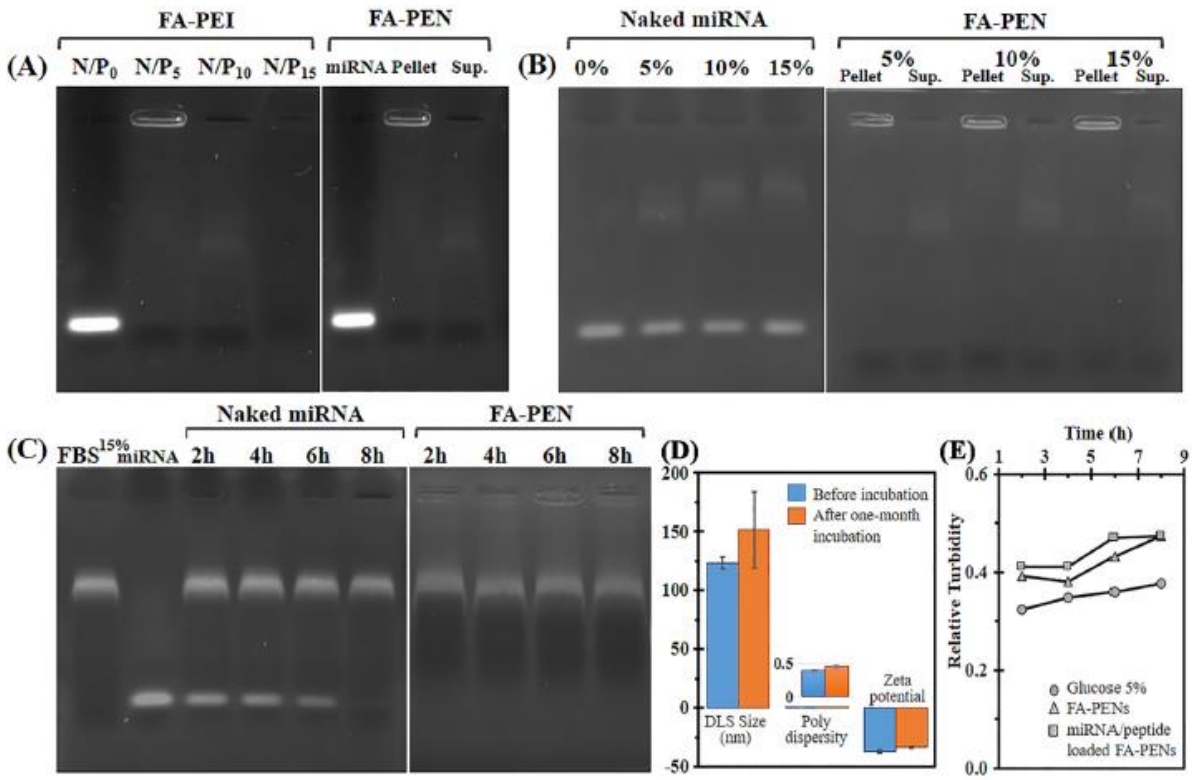

Fig. 3. (A) Gel retardation assay of miRNA in FA-PEI with various N/P ratios (w/w) and FA-PENs at N/P ratio of 150 (w/w) after centrifugation; (B) In vitro serum stability of naked miRNA and miRNA-loaded FA-PENs at the N/P ratio of 150 (w/w) in the presence 5%, 10%, 15% serum for 30 min were assessed by agarose gel electrophoresis; (C) In vitro serum stability of naked miRNA and miRNA-loaded FA-PENs at the N/P ratio of 150 (w/w) in 15% serum for 2, 4, 6 and 8 h, respectively. Lane 1, 15% serum and Lane 2, miRNA in the absence of serum; (D) In vitro stability of FA-PENs and miRNA/peptide loaded FA-PENs in glucose 5% solution; (E) In vitro stability of FA-PENs and Co-loaded FA-PENs against Glucose 5%.

Additionally, serum stability of the particles is another significant concern because the negatively charged components in serum will interact nonspecifically with positively charged nanocarriers that lead to faster opsonization and loss of predicted therapeutic effects [**36**]. In this study, the serum stability of the particles was determined by measuring the turbidity as a function of time. Changes in particle size and concentration affect particle aggregation that can be observed as changes in suspension turbidity. As shown in **Fig. 3E** there was no significant increase of turbidity in FA-PENs and miRNA/peptide-loaded FA-PENs suspensions after incubating in FBS for 8 h as well as that of glucose 5% solution. It was suggested that the repulsion forces among the nanocarrier with high negative zeta potential and the negatively charged plasma proteins prevent particle aggregation.

3.4. Cellular uptake of PENs and FA-PENs

Successful effects of drug-loaded nanocarriers significantly depend on permeability and retention of nanotherapeutics in the target cells, which will be determined by specific properties of the carriers such as passive and/or active targeting [37]. In passive targeting, physical properties such as size, functional groups, charge, and hydrophilicity of the surface will improve drug efficacy, half-life, and safety profiles through the enhanced permeability and retention effect [**38**]. In active targeting, the surface of a nanocarrier is typically conjugated by a targeting moiety with superior specificity [**37**]. FA

is known as a ligand with high affinity to the FA receptors that are overexpressed in cancer cells and improves therapeutic targeting against them [**39**].

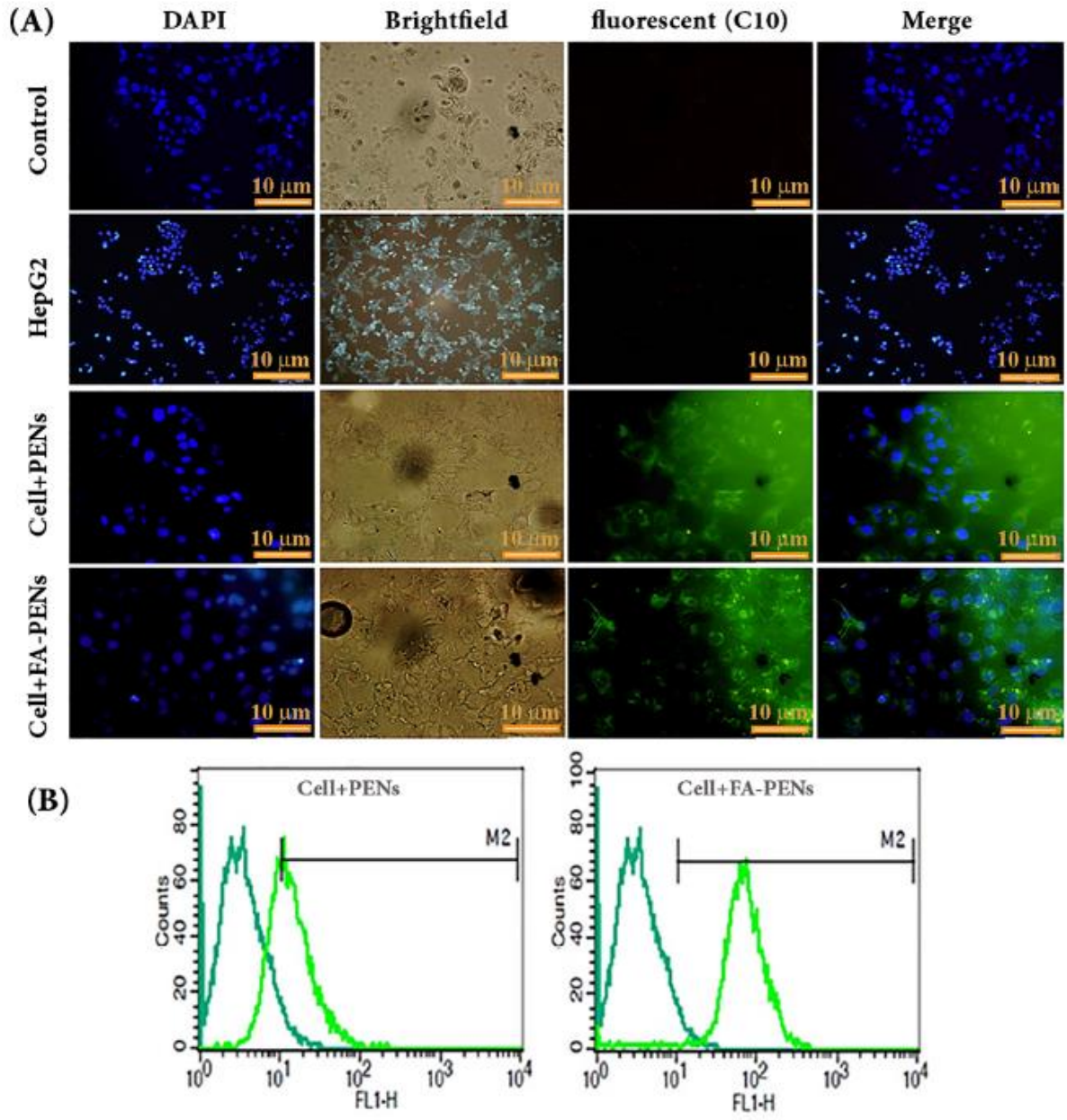

Fig. 4. Cellular uptake of nanocarriers by MDA-MB-231 cells in compared to HepG2 as negative control after 2 h incubation with C10-loaded targeted and nontargeted nanocarriers at 37 °C. (A) Evaluation by fluorescence microscopy and (B) measurement of fluorescence signals by flow cytometry.

Moreover, equipping the surface of the nanocarriers with folic acid increases their cellular uptake via endocytosis. However there are some papers exposed cells to free NPs and FA-NPs in the absence and presence of free folic acid [**40,41**] to quantify the uptake of folate-targeted nanoparticles via folate receptors, different studies also evaluated in vitro cellular uptake of nanoparticles on various cell lines in the absence of free folic acid [**42.43**] . Herein, cellular uptake of targeted (FA-PENs) and non-targeted (PENs) nanocarriers were evaluated by fluorescence microscopy and flow cytometry in the absence of free folic acid. In order to show specificity of FA-PEN respect to FA-receptors, HepG2 cell

line was selected and the uptake of FA-PEN was analyzed, the relevant data was shown in **Fig. 4A**. Therefore, the FA was grafted over the PEI strand, and accordingly, the cellular uptake efficiency of fluorescent PENs and FA-PENs was compared after 2 h incubation by MDA-MB-231 cells. For this purpose, a synthetic fluorescence marker, phenylxanthene dye (C10), has been used. The results were shown in **Fig. 4A**. In fluorescence microscopy images, the green fluorescence of the C10-loaded nanocarriers accumulated around nuclei (DAPI stained blue) showed the internalization of nanocarriers. A comparison between the fluorescent view of HepG2 and the control line shows that most internalization is specific due to FA attachment. The quantitative analysis of uptake was performed using flow cytometry by which the ability of FA-PENs was measured to be up to 98.04 ± 1.45 compared to that of PENs, which was about 63.49 ± 4.09. The high uptake efficiency of the PENs, especially for MDA-MB-231 cell line with its multidrug resistance properties, is surprising, which can be attributed to some of its physical properties, including spherical shape and small size along with high surface charge [**38.44**]. So, it can be concluded that active targeting will increase cellular uptake by two strategies including enhanced permeability and retention (EPR) effect, and specific interactions between the FA-PENs and FA receptors that are expressed significantly more at the surface of cancer cells than normal cells.

3.5. Release and toxicity behavior

Various factors including physicochemical properties of the nanocarriers (i.e., shape, size, composition, hydrophobicity and surface charge), biological parameters (i.e., diversities in the responsive site including endosome, lysosome, cytosol, or nucleus) and exposure conditions (i.e., particle concentration, medium composition, and temperature) influence the release rate and cytotoxicity of nanocarriers [**45,46**]. Since the drug release pattern of the nanocarriers is one of the most effective parameters, the in vitro release profile of the BSA-loaded FA-PENs was investigated under a release medium (PBS 10 mM, pH 7.4) at 37 °C. Although the BSA is larger than the Mel and LTX-315, due to restrictions on providing these peptides, BSA was used as a peptide cargo model with an isoelectric point of 4.7 [**47**]. As shown in **Fig. 5A**-solid line, the in vitro release was assigned to a biphasic process, including a burst release (0-6 h), which continued with a subsequent gradual release of 95% for 96 h. Moreover, the in vitro release model was selected through the correlation coefficient value (r^2) of different models, including zero-order, first-order, Higuchi, Hixson-Crowell's, and Korsmeyer-Peppas kinetics at two phases including burst and gradual release (data not shown). Regarding r^2 and the multilayer structure of the carrier, Korsmeyer-Peppas' kinetic model was selected for two phases (r^2 = 0.9981, n = 2.9258, and r^2 = 0.9736, n = 0.4338 for burst and gradual phase, respectively), which is further confirmed by the linear relationship between the logarithm of the release percentage and the logarithm of the release time shown in **Fig. 5A**-dotted line. So, according to the available model for the multilayer structure of the carrier, the mechanism was discussed by non-Fickian (Super case II) in the initial phase and subsequently Quasi Fickian transport during the remaining phase owing to the exponent “n”. In the first stage, the solvent diffuses into the carrier with high acceleration, leads to tension, breaking and relaxation of the polymers (solvent crazing), and in turn, release of BSA. In the second phase, BSA release is governed significantly by diffusion, so that the solvent diffuses into the matrix more rapidly than the polymeric relaxation, which leads to equilibrium and time-dependent manner (release pattern). In an intracellular release, it is considered that the nanocarriers are generally deformed by swelling or disrupted by dissolution or polymer degradation under acidic endo/lysosomal conditions [**48**].

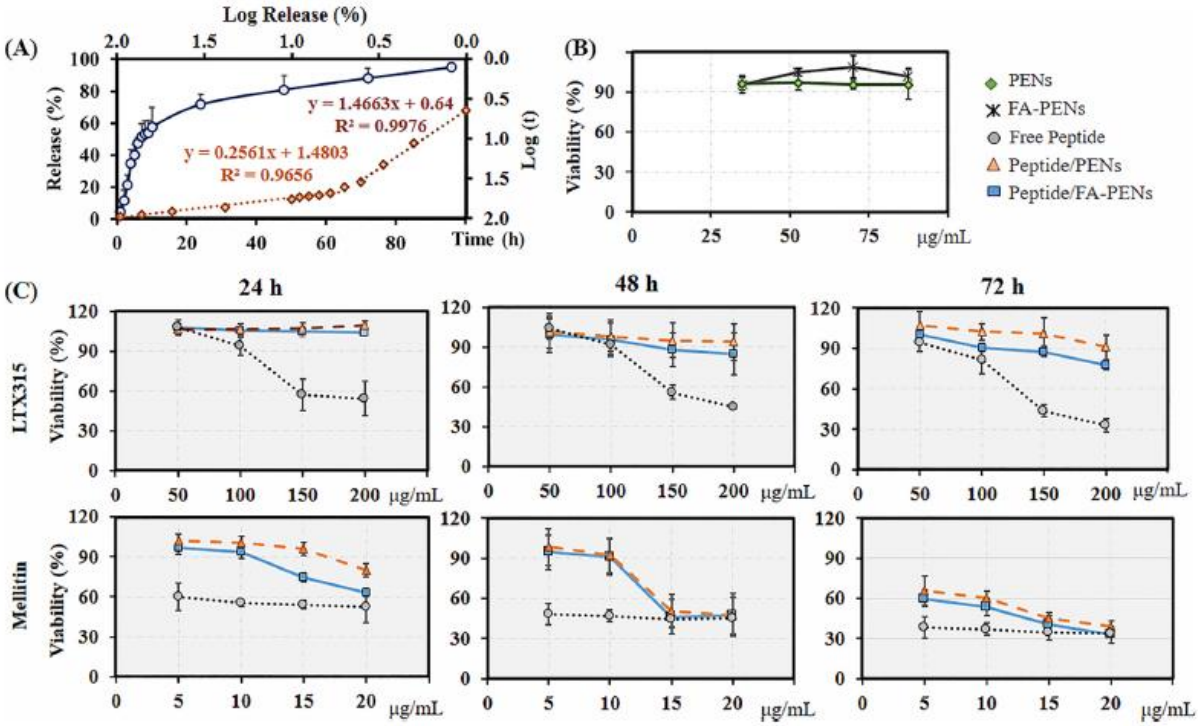

Fig. 5. (A) In vitro release profile of the BSA-loaded FA-PENs in PBS, pH 7.4 at 37 °C. (B) Biocompatibility of FA-PENs and PENs at different concentrations (35, 52.5, 70 and 87.5 pg/mL) for 24 h. (C) Time-monitoring of cell viability of MDA-MB-231 cells in presence of LTX- and Mel-loaded nanocarriers at different concentrations compared to free LTX-315 and Mel, respectively.

Nonetheless, the possible “proton sponge effect” of PEI leads to high buffering capability at low pH through the protonation of tertiary amines, promoting an influx of protons inside the acidic cellular compartments and the consequent rupture of the organelle membrane due to an osmotic imbalance. Therefore, it can be a promising strategy for promoting the release of genetic material from the acidic vesicles and, thus, facilitating the incoming to the nucleus [**15,49**].

For a deep understanding of the release pattern of the peptides, the cytotoxicity of PENs and FA-PENs in the presence and absence of peptides was investigated using MTS assay at three-time points of 24, 48, and 72 h. As depicted in **Fig. 5B**, unloaded nanocarriers, targeted and non-targeted, did not show any toxicity on MDA-MB-231 cells due to their sphere-shape, high negative charge, and small size as well as using biocompatible polymers [**45,46**]. Slightly higher cell viability of FA-PENs compared to PENs is attributed to the use of folic acid, which acts as a driving force for growth, proliferation, and survival, through providing DNA-precursor, DNA repairing, and methylation [**50**]. Besides, the ligand/receptor internalization process did not damage the integrity of the plasma membrane and exhibited milder cytotoxic effects. **Fig. 5C** also demonstrated the toxicity effects of free LTX-315 and Mel in comparison with loading PENs and FA-PENs at different concentrations at three-time points of 24, 48, and 72 h. According to **Fig. 5C**, Mel showed significantly higher toxicity than LTX-315, which can be attributed to the carrier release pattern in this fashion: 1) during 24 h, despite the toxicity effect of free Mel and LTX-315 at concentrations higher than 5.0 and 150 |ig/mL, respectively, only Mel-loaded nanocarriers showed cytotoxicity effect. This is consistent with the fact that the amount of released peptides are less than the IC50 level, and the effectiveness of Mel is greater than LTX-315, 2) at 48 h, LTX-315 loaded nanocarriers started killing the cells, but the concentration of released LTX-315 was lower than the

IC50 concentration, while the released Mel at concentrations above 15 ig/mL reduced the cell viability more than 50%, 3) within 72 h, the release and cytotoxicity effect of Mel and LTX-315 continued with a gentle slope, and 4) there was no significant difference between cytotoxicity effect of peptide-loaded PENs and FA-PENs. According to this cytotoxicity pattern, the release of peptide-loaded nanocarrier is time-dependent and starts after 12 h with a 10% release and lasts with a 95% release up to 72 h. Although the release rate is proportional to the initial load of the peptide, the release pattern is repetitive and in accordance with the BSA-model. Overall, the type, size, and charge of the peptides influence release rate and in turn, cytotoxic effects, which is acceptable for nanocarriers with a polyelectrolyte structure whose electrostatic interaction plays an important role in the stability and integrity of the carriers [**51**].

Since the release of peptide-loaded into the core occurs after the disintegration of the shell, the maximum release of miR-34a occurs at the first 24 h. However, the MTS assay confirmed that the 100 nM free miR-34a only reduced the viability of MDA-MB-231 cell line by 10% over 48 h, which is consistent with its multidrug resistance properties. This caused the single loading of miR-34a on PENs, and FA-PENs did not essentially affect cell viability (data not shown).

3.6. Cell cycle analysis

To confirm the synergistic effect of simultaneous delivery of cargos, miR34-a, and peptides, the cell cycle assay was performed in terms of overcoming the multidrug resistance and induction of death pathways, especially apoptosis. In normal cells, the cell cycle transition phases are controlled by a complex series of signaling pathways to correct errors or commit suicide (apoptosis) along with cell cycle arrest. While the cancerous cells, as a result of genetic mutations, defect in the regulatory process leading to uncontrolled cell proliferation. So, it is expected that the controlled induction of cell cycle arrest and apoptosis plays a key role in controlling cancer cell proliferation. Successful arrest in G1 and S phases, as well as G2 and mitosis, increases the cell percentage in the first two stages and decreases the cells in the second two stages [**52**]. Therefore, the effect of cargos-loaded nanocarriers on cell cycle perturbation was compared with unloaded nanocarriers by flow cytometry using propidium iodide.

Fig. 6A shows the cell cycle parameters of MDA-MB-231 treated with FA-PENs as a control, and peptides, miRNA, and miRNA/peptide-loaded FA-PENs. Obviously, the cell cycle parameters in G2 phase were perturbed in favor of increasing the G1 phase after treating with all cargos, and S phase in the presence of miR-34a. However, the amount and portion of each phase in this turbulence depends on the cargo quantified in **Fig. 6B**. Accordingly, single or co-delivery of miR-34a increased DNA duplication and the cell percentage in the S phase, which is consistent with Wang et al. [**52**]. They demonstrated that miR-34a directly targeted tRNAiMet precursors that promoted cell proliferation, inhibited apoptosis, and accelerated the S/G2 transition [**52**]. While the delivery of peptides, LTX-315 and Mel, reduced DNA synthesis at S phase and increased G1/S transition, which led to the cell cycle arrest. Probably, LTX-315 displayed a similar anticancer activity in breast as well as head and neck cancers by inhibiting cell cycle progression in G1/S transition. Surprisingly, co-delivery reduced the cells inG2-phase significantly compared to single delivery, particularly miR-34a/Mel/FA-PENs, which confirmed their synergistic effect in inducing death pathways by more than 59%. Different studies also confirmed that miR-34a and Mel stimulate cell cycle arrest through the downregulation of cyclin D1 and inhibition of inappropriate cell proliferation in the G1 phase [**53-55**].

Cell cycle arrest is a regulatory process governed by the dynamic activities of protein complexes, including Akt, p21, p19, p27, Cdk2, cyclin E, Cdk4, and cyclin D1 [**56**]. The core of each complex comprises a cyclin and a cyclin-dependent kinase (CDK). Cyclin D1 is a member of the cyclin D-group,

which acts as a controller of a cell cycle progression in the transition from G1 into S phase [**57**]. Therefore, the expression of Cyclin D1 was evaluated at both mRNA and protein levels using qRT-PCR and western blot. As shown in **Fig. 6C**, the mRNA and protein expression levels of Cyclin D1 were decreased in the presence of Mel and miR-34a compared to the untreated cells. The co-treatment by Mel/miR-34a also clearly revealed their synergistic effect by a significant decrease in the mRNA and protein levels. Low expression of Cyclin D1 in the presence of miR-34a was also compatible with previous studies in breast cancer cell lines, which resulted in a significant reduction in cell proliferation and apoptosis promotion [**58,59**]. However, by using LTX-315/FA-PENs, mRNA expression of Cyclin D1 was very vague because of the higher expression of GAPDH than the test genes (data not shown).

3.7. Cell death by apoptosis

Apoptosis, a genetically programmed cell death, occurs as a defense mechanism during development and aging of cells. Cell shrinkage, membrane blebbing, chromatin cleavage and nuclear condensation are a few common features of apoptosis [**57**]. Therefore, DAPI staining was used to demonstrate the effect of apoptosis on the chromatin morphology of the cells after 24 and 48 h. As shown in **Fig. 7A**, the chromosome condensation (represented by red arrow) was significantly increased in co-treated cells in a time-dependent manner. So, the gradual alterations in the morphology of the treated cells and the synergistic effect of the cytotoxic agents clearly indicated the evidence of apoptosis, which was consistent with the gradual release of the cargos.

To demonstrate the correlation of the chromatin morphology of the cells with their biochemical properties, expression of Bcl-2 at mRNA and protein levels, and then caspase-8 activity were evaluated. The Bcl-2 family of proteins such as antiapoptotic Bcl-2, the effector proapopto-tic proteins, and BH3-only proteins can activate or inhibit apoptosis by interacting with each other and determine cell fate [**60**]. Bcl-2 is the first identified antiapoptotic 24 kDa protein localized mainly in the membranes of the mitochondria and endoplasmic reticulum. It inhibits the apoptotic process by regulating Ca^{2+} homeostasis, preventing cytochrome *c* release, neutralizing Bax function, and blockade of caspase activation [**61,62**]. In other words, the activation of caspase proteins is another important factor contributing to apoptosis induction by extrinsic and/or intrinsic pathways [**63**]. Caspases as a group of cysteine proteases are classified into initiators (e.g., caspase-8 and 9) and effector (e.g., caspase-3, 6, and 7). Caspase-8 is the most apical caspase in death receptor-mediated apoptosis that is activated by the extrinsic pathway [**63**].

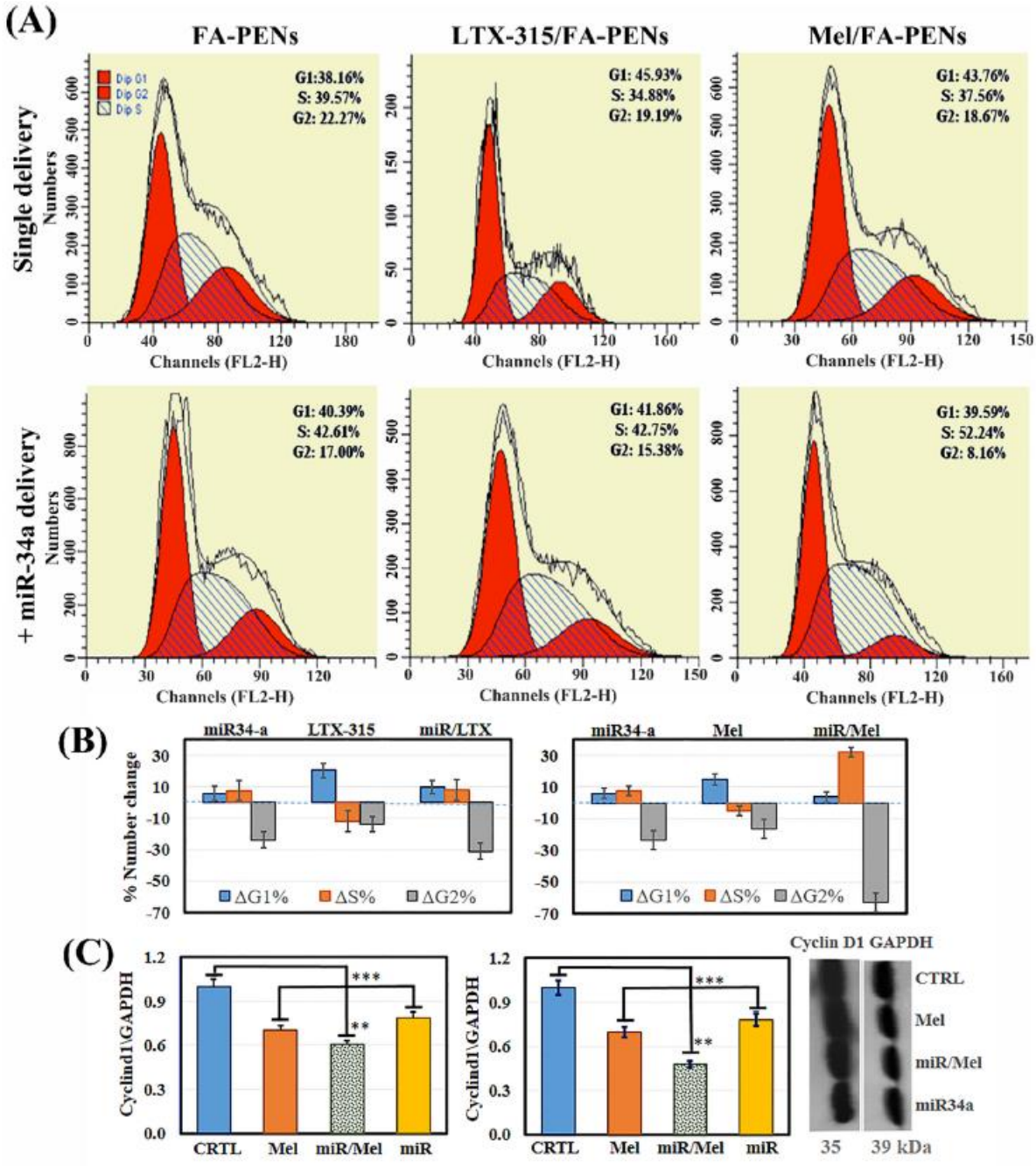

Fig. 6. (A) Cell cycle parameters of MDA-MB-231 treated with FA-PENs as control and peptides (LTX-315 and Mel), miRNA and miRNA/peptide-loaded FA-PENs. (B) Quantitative representation of cell cycle parameters reported in part A. (C) Evaluation of Cyclin D1 effect on mRNA and protein expression after treatment with Mel, Mel/FA-PENs and miR-34a-Mel/PENs. The significant difference between the groups was analyzed by $p < 0.1$ and <0.01 represented by ** and ***, respectively. Concentration of miR-34a, LTX-315 and Mel were constant in all experiments, 100 nM, 150 pg/mL and 15 pg/mL, respectively.

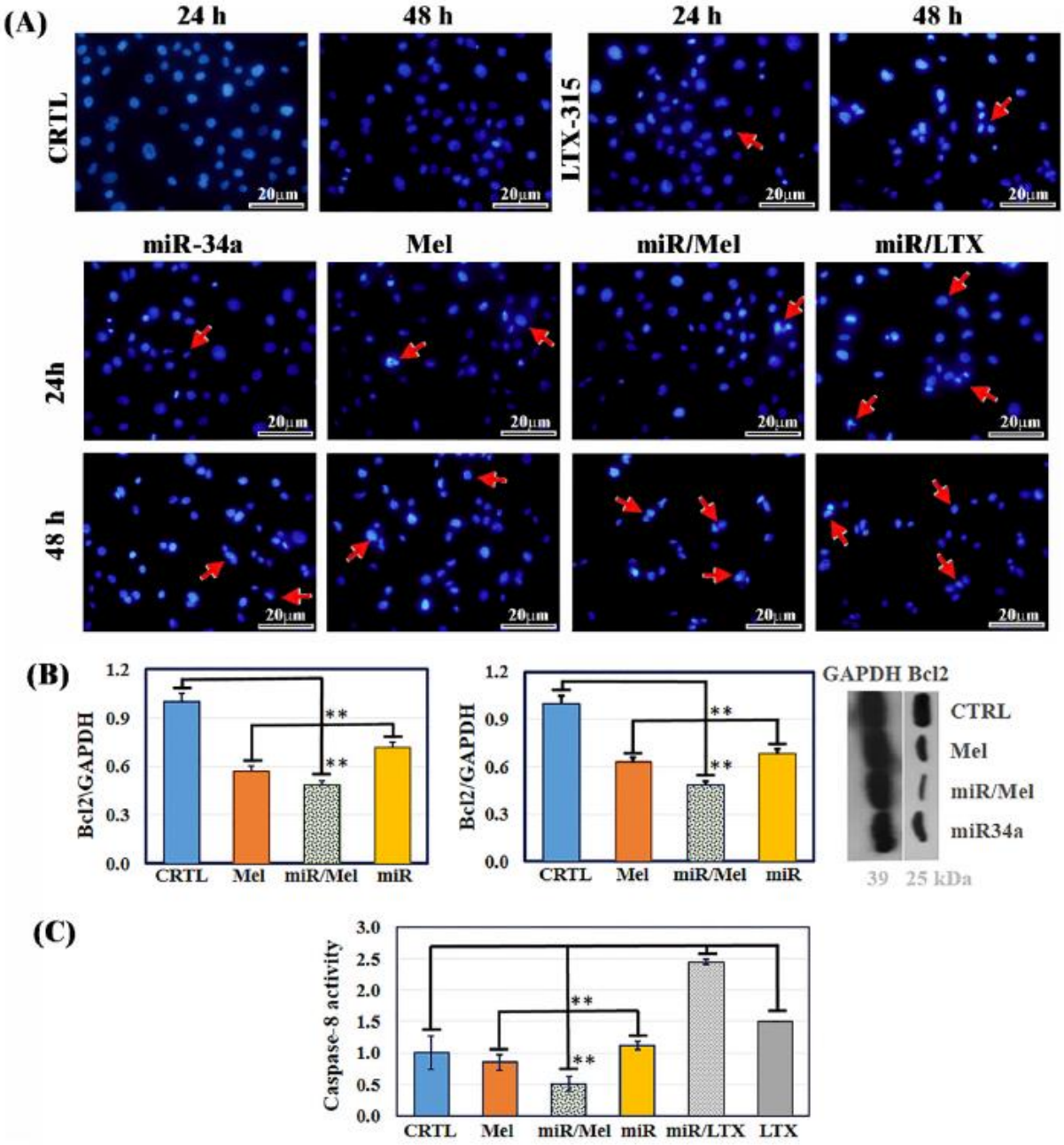

Fig. 7. MDA-MB-231 apoptosis after treatment by miR-34a, LTX-315, miR-34a/LTX-315, Mel and miR-34a/Mel. (A) DAPI staining of MDA-MB-231 cancer cells at two time points of 24, 48 h. The chromosome condensation was represented by red arrow. (B) Evaluation of anti-apoptotic effect of Bcl-2 at both the mRNA and protein levels after treatment with Mel, Mel/FA-PENs and miR-34a-Mel/PENs. (C) Colorimetric assay of caspase-8 activity. The significant difference between the groups was analyzed by$p < 0.1$ and <0.01 represented by ** and ***, respectively. Concentration of miR-34a, LTX-315 and Mel were constant in all experiments and were 100 nM, 150 pg/mL and 15 pg/mL respectively. (For interpretation of the references to color in this figure legend, the reader is referred to the web version of this article.)

However, **Fig. 7B** demonstrated that the mRNA and protein expression levels of Bcl-2 were decreased in the presence of Mel and miR-34a compared to untreated cells. The co-treatment by Mel/miR-34a clearly revealed their synergistic effect by a significant decrease in the mRNA and protein levels. The results were in agreement with the previous studies that stated that Mel inhibited STAT3 activation, prevented translocation of NF-kB p65 into the nucleus, and improved expression of antiapoptotic genes such as Bcl-2, cyclin D1, CDK4 and mitochondrial cytochrome *c* [**64-66**]. Gajski et al. also

introduced Bcl-2 as a key regulator in Mel-induced apoptosis in human leukemic cells, which was controlled through the Akt signaling pathway [67]. Low expression of Bcl2 in the presence of miR-34a was also compatible with previous studies in breast cancer cell lines resulted in a significant reduction in cell proliferation and promotion of apoptosis [**58,59**]. However, by using LTX-315/FA-PENs, mRNA expression of Bcl-2 was very vague because of the higher expression of GAPDH than the test genes (data not shown). Perhaps LTX-315 affects the expression of these genes partially, but according to Zhou et al., the cells without two proapoptotic multidomain proteins from the Bcl-2 family, BAX and BAK, are less susceptible to LTX-315-mediated killing. This showed that the main mechanism of cell death by LTX-315 is immunogenic cell death, which occurred through the permeabilization of mitochondrial membranes and necrosis [**6**].

Finally, the colorimetric assay of caspase-8 showed a significantly elevated caspase-8 activity in MDA-MB-231 cells treated with miR-34a, LTX-315, and miR-34a/LTX-315, but markedly reduced in the presence of Mel and Mel/miR-34a compared with untreated cells (**Fig. 7C**). In this regard, caspase-8 involved in the extrinsic receptor-dependent pathway LTX-315, possibly induces the apoptotic pathway in an extrinsic way. This high caspase-8 activity of LTX-315 contradicts the evidence regarding its caspase-independent necrosis [**6**]. Zhou et al. proved that LTX-315 mediated immunogenic cell death by permeabilization of mitochondrial membranes and massive release of HMGB1 from the nuclei of dead cells, as well as caspase-3 activation in a fraction of the cells [**6**]. Nonetheless, decreased level of caspase-8 in Mel treated cells indicated that apoptosis might occur via a suppression of intrinsic way. Our results were consistent with the studies that confirmed the role of Mel in the induction of apoptosis by the cleavage of caspase-3 and -9 [**64,67**], but not caspase-8 [**67**].

4. Conclusions

In the present study, novel targeted nanocarriers were successfully designed and prepared by Layer-by-layer self-assembly of oppositely charged layers. They include CS-PGA, DS, and FA-PEI for co-delivery of different cytotoxic agents (LTX-315, Mel, and miR-34a). The use of the polymers has been explored due to their interesting features such as exhibition of specific sites for drug attachment, the ability to be functionalized through the addition of specific chemical groups, and degradability. The core was greatly explored as an efficient peptide carrier, and the shell was used for its potential in gene delivery technology. These Layer-by-layer nanocarriers showed acceptable stability, high encapsulation efficiency, and targeted to specific cells. Cytotoxic studies showed that the nanocarriers did not affect the viability of the target cells, but the peptides demonstrated time-dependent cytotoxicity, which probably confirmed their gradual release. Low caspase-8 activity, gene knockout of Bcl-2, and Cyclin D1 by Mel/miR-34a clearly exhibited the synergistic effect of Mel and miR-34a on apoptosis and cell cycle arrest. Nonetheless, high caspase-8 activity and unclear gene expressions of the cells in the presence of LTX-315 showed a different pathway of apoptosis. DAPI staining assay clearly confirmed the apoptotic effect of the cytotoxic agents. On the whole, the results of this work suggest that the constructed nanocarriers have a significant potential for co-delivery of cytotoxic agents that exert different mechanisms of action. Owing to the use of this kind of nanocarrier in the development of therapies against cancer, the in vivo antitumor efficacy is considered in the subsequent study.

Abbreviations

LTX LTX-315

Mel Melittin

MDA-MB-231

miR miR-34a

MDR Multidrug resistence

PENs Polyelectrolyte nanocarries

CS Chitosan

PGA Polyglutamic acid

TTP Tripolyphosphate

DS Dextran sulfate

PEI Polyethyleneimine

FA Folic acid

PGA-CS PGA grafted CS

FA-PEI FA grafted PEI

EE Encapsulation effciency

LC Loading capacity

References

[1] G. Pistritto, D. Trisciuoglio, C. Ceci, A. Garufi, G. D'Orazi, Aging (Albany NY) 8 (2016) 603.

[2] Y. Ding, W. Liu, W. Yu, S. Lu, M. Liu, D.L. Kaplan, X. Wang, J. Tissue Eng. Regen. Med. 12 (2018) 1959-1971.

[3] S. Shi, L. Han, L. Deng, Y. Zhang, H. Shen, T. Gong, Z. Zhang, X. Sun, J. Control. Release 194 (2014) 228-237.

[4] X. Lin, W. Chen, F. Wei, B.P. Zhou, M.-C. Hung, X. Xie, Theranostics 7 (2017) 4805.

[5] B. Sveinbjornsson, K.A. Camilio, B.E. Haug, 0. Rekdal, Future Med. Chem. 9 (2017) 1339-1344.

[6] H. Zhou, S. Forveille, A. Sauvat, T. Yamazaki, L. Senovilla, Y. Ma, P. Liu, H. Yang, L. Bezu, K. Muller, Cell Death Dis. 7 (2016), e2134.

[7] H.N. Lim, S.B. Baek, H.J. Jung, Molecules 24 (2019) 929.

[8] M. Hematyar, M. Soleimani, A. Es-Haghi, A.J.A.c. Rezaei Mokarram, Nanomed. Biotechnol. 46 (2018) S1226-S1235.

[9] K.A. Camilio, M.-Y. Wang, B. Mauseth, S. Waagene, G. Kvalheim, 0. Rekdal, B. Sveinbjornsson, G.M. Maelandsmo, Breast Cancer Research 21 (2019) 1-12.

[10] M. Motiei, V. Sedlařík, L.A. Lucia, H. Fei, L. Munster, Carbohydr. Polym. (2019), 115709.

[11] M. Motiei, S. Kashanian, Eur. J. Pharm. Sci. 99 (2017) 285-291.

[12] M. Motiei, S. Kashanian, A. Taherpour, Drug Dev. Ind. Pharm. 43 (2017) 1-11.

[13] I.R. Khalil, A.T. Burns, I. Radecka, M. Kowalczuk, T. Khalaf, G. Adamus, B. Johnston, M.P. Khechara, Int. J. Mol. Sci. 18 (2017) 313.

[14] J.-S. Lee, H.G. Lee, Int. J. Biol. Macromol. 85 (2016) 9-15.

[15] M.-M. Xun, Z. Huang, Y.-P. Xiao, Y.-H. Liu, J. Zhang, J.-H. Zhang, X.-Q. Yu, Polymers 10 (2018) 1060.

[16] K. Siwowska, R.M. Schmid, S. Cohrs, R. Schibli, C. Muller, Pharmaceuticals 10 (2017) 72.

[17] S.V. Lale, A. Aravind, D.S. Kumar, V. Koul, Biomacromolecules 15 (2014) 1737-1752.

[18] M. Motiei, S.Z. Mirahmadi-Zare, M.H. Nasr-Esfahani, Biophys. Chem. 275 (2021) 106605.

[19] W. Wang, W. Li, J. Wang, Q. Hu, M. Balk, K. Bieback, C. Stamm, F. Jung, G. Tang, A. Lendlein, Clin. Hemorheol. Microcirc. (2017) 1-17.

[20] S.V. Mussi, G. Parekh, P. Pattekari, T. Levchenko, Y. Lvov, L.A. Ferreira, V. P. Torchilin, Int. J. Pharm. 495 (2015) 186-193.

[21] T. López-León, E. Carvalho, B. Seijo, J. Ortega-Vinuesa, D. Bastos-González, J. Colloid Interface Sci. 283 (2005) 344-351.

[22] Y. Wang, G. He, Z. Li, J. Hua, M. Wu, J. Gong, J. Zhang, B. Li-tong, L. Huang, Polymers 10 (2018) 112.

[23] L.-L. Wang, J.-T. Chen, L.-F. Wang, S. Wu, G.-z. Zhang, H.-Q. Yu, X.-d. Ye, Q.-S. Shi, Sci. Rep. 7 (2017) 12787.

[24] C. Krejtschi, K. Hauser, Eur. Biophys. J. 40 (2011) 673-685.

[25] C.L. Pereira, J.C. Antunes, R.M. Gonęalves, F. Ferreira-da-Silva, M.A. Barbosa, J. Mater. Sci. Mater. Med. 23 (2012) 1583-1591.

[26] J. Xu, D. Solaiman, R.D. Ashby, R.A. Garcia, S.H. Gordon, R.E. Harry-O'kuru, Starch-Starke 69 (2017), 1600021.

[27] S. Lakard, G. Herlem, B. Lakard, B. Fahys, J. Mol. Struct. THEOCHEM 685 (2004) 83-87.

[28] I. Yudovin-Farber, N. Beyth, E.I. Weiss, A.J. Domb, J. Nanopart. Res. 12 (2010) 591-603.

[29] J. Varshosaz, F. Hassanzadeh, H. Sadeghi Aliabadi, M. Nayebsadrian, M. Banitalebi, M. Rostami, Biomed. Res. Int. 2014 (2014).

[30] C. Chavan, P. Bala, K. Pal, S. Kale, OpenNano 2 (2017) 28-36.

[31] G.S. Nikolic, M.D. Cakic, S. Glisió, D.J. Cvetkovic, Ž.J. Mitic, D.Z. Markovic, Study of green nanoparticles and biocomplexes based on exopolysaccharide by modern Fourier transform spectroscopy, in: Fourier Transforms-High-tech Application and Current Trends, InTech, 2017.

[32] A. Patel, R. Gaudana, A.K. Mitra, J. Microencapsul. 31 (2014) 542-550.

[33] Y. Zeng, Z. Zhou, M. Fan, T. Gong, Z. Zhang, X. Sun, Mol. Pharm. 14 (2016) 81-92.

[34] L. Zhang, X. Yang, Y. Lv, X. Xin, C. Qin, X. Han, L. Yang, W. He, L. Yin, Sci. Rep. 7 (2017) 46186.

[35] H. Jonassen, A.-L. Kj0niksen, M. Hiorth, Biomacromolecules 13 (2012) 3747-3756.

[36] Q. Feng, M.-Z. Yu, J.-C. Wang, W.-J. Hou, L.-Y. Gao, X.-F. Ma, X.-W. Pei, Y.-J. Niu, X.-Y. Liu, C. Qiu, Biomaterials 35 (2014) 5028-5038.

[37] M. Motiei, S. Kashanian, L.A. Lucia, M. Khazaei, J. Control. Release 260 (2017) 213-225.

[38] K. Kettler, K. Veltman, D. van de Meent, A. van Wezel, A.J. Hendriks, Environ. Toxicol. Chem. 33 (2014) 481-492.

[39] H. Jin, J. Pi, F. Yang, J. Jiang, X. Wang, H. Bai, M. Shao, L. Huang, H. Zhu, P. Yang, Sci. Rep. 6 (2016) 30782.

[40] S. Dong, H.J. Cho, Y.W. Lee, M. Roman, Biomacromolecules 15 (2014) 1560-1567.

[41] S.-J. Yang, F.-H. Lin, K.-C. Tsai, M.-F. Wei, H.-M. Tsai, J.-M. Wong, M.-J. Shieh, Bioconjug. Chem. 21 (2010) 679-689.

[42] Z.C. Soe, W. Ou, M. Gautam, K. Poudel, B.K. Kim, L.M. Pham, C.D. Phung, J.-H. Jeong, S.G. Jin, H.-G. Choi, Pharmaceutics 11 (2019) 562.

[43] L. Cheng, H. Ma, M. Shao, Q. Fan, H. Lv, J. Peng, T. Hao, D. Li, C. Zhao, X. Zong, Mol. Med. Rep. 16 (2017) 1101-1108.

[44] E. Gullotti, Y. Yeo, Mol. Pharm. 6 (2009) 1041-1051.

[45] E. Frohlich, Int. J. Nanomedicine 7 (2012) 5577.

[46] Y.-W. Huang, M. Cambre, H.-J. Lee, Int. J. Mol. Sci. 18 (2017) 2702.

[47] R. Li, Z. Wu, Y. Wangb, L. Ding, Y. Wang, Biotechnol. Rep. 9 (2016) 46-52.

[48] F. Meng, R. Cheng, C. Deng, Z. Zhong, Mater. Today 15 (2012) 436-442.

[49] B. Fortuni, T. Inose, M. Ricci, Y. Fujita, I. Van Zundert, A. Masuhara, E. Fron, H. Mizuno, L. Latterini, S. Rocha, Sci. Rep. 9 (2019) 1-13.

[50] S.Y. Hwang, Y.J. Kang, B. Sung, J.Y. Jang, N.L. Hwang, H.J. Oh, Y.R. Ahn, H. J. Kim, J.H. Shin, M.a. Yoo, J. Cell. Physiol. 233 (2018) 736-747.

[51] M. Motiei, V. Sedlařík, L.A. Lucia, H. Fei, L. Munster, Carbohydr. Polym. 231 (2020), 115709.

[52] B. Wang, D. Li, I. Kovalchuk, I.J. Apel, A.M. Chinnaiyan, R.K. Wóycicki, C. R. Cantor, O. Kovalchuk, Proc. Natl. Acad. Sci. 115 (2018) 7392-7397.

[53] F. Sun, H. Fu, Q. Liu, Y. Tie, J. Zhu, R. Xing, Z. Sun, X. Zheng, FEBS Lett. 582 (2008) 1564-1568.

[54] A. Williams, Cell. Mol. Life Sci. 65 (2008) 545.

[55] Z. Yang, T. Zhang, Q. Wang, H. Gao, Mol. Ther. Oncol. 10 (2018) 40-47.

[56] C. Chea, M. Miyauchi, T. Inubushi, N.F. Ayuningtyas, A. Subarnbhesaj, P. T. Nguyen, M. Shrestha, S. Haing, K. Ohta, T. Takata, PLoS One 13 (2018), e0191683.

[57] S. Radovic, M. Babic, M. Dorió, A. Hukió, S. Kuskunovic, A. Hadžismajlovic,F. Serdarevió, Bosnian J. Basic Med. Sci. 7 (2007) 205.

[58] A. Campos-Parra, G. Mitznahuatl, A. Pedroza-Torres, R. Romo, F. Reyes, E. López-Urrutia, C. Pórez-Plasencia, Int. J. Mol. Sci. 18 (2017) 1182.

[59] L. Kastl, I. Brown, A.C. Schofield, Breast Cancer Res. Treat. 131 (2012) 445-454.

[60] O.N. Sivrikoz, G. Kandiloglu, Iran. J. Pathol. 10 (2015) 185.

[61] M.C. Pratt, M.-Y. Niu, J. Biol. Chem. 278 (2003) 14219-14229.

[62] H. Lin, Y. Lee, G. Li, R. Pestell, H. Kim, Cell Death Differ. 8 (2001) 44.

[63] B. Fischer, D. Coelho, P. Dufour, J.-P. Bergerat, J.-M. Denis, J. Gueulette, P. Bischoff, Biochem. Biophys. Res. Commun. 306 (2003) 516-522.

[64] S.-K. Kim, K.-Y. Park, W.-C. Yoon, S.-H. Park, K.-K. Park, D.-H. Yoo, J.-Y. Choe, Joint Bone Spine 78 (2011) 471-477.

[65] J.E. Yoon, K. Hong, S.G. Han, Curr. Top. Nutraceut. Res. 16 (2018).

[66] H. Zhang, B. Zhao, C. Huang, X.-M. Meng, E.-B. Bian, J. Li, PLoS One 9 (2014), e95520.

[67] G. Gajski, V. Garaj-Vrhovac, Environ. Toxicol. Pharmacol. 36 (2013) 697-705.